


Local alkalinity enables high-performance pure water anion exchange membrane electrolysis

Received: 16 August 2025

Accepted: 25 January 2026

Published online: 04 February 2026

 Check for updatesJiixin Guo^{1,2,6}, Ruguang Wang^{1,2,6}, Yuting Yang³✉, Qinshao Zhang⁴,
Fahe Cao⁴, Jiong Zhao⁵, Caofeng Pan¹✉ & Tao Ling²✉

Anion exchange membrane water electrolyser is a highly promising electrolyser technology, but its performance in pure water is severely limited by the unsatisfactory OH⁻ conductivity of the membrane. To overcome this critical challenge, we develop a local alkalinity engineering strategy that employs TiO₂ nanoparticles in catalyst layers. These nanoparticles enrich OH⁻ in the electric double layer at both electrodes, creating self-sustaining alkaline micro-environments (pH ~ 14), as confirmed by a scanning electrochemical microscopy technique integrating pH microelectrodes. As a result, the engineered electrolyser achieves a high current density of 3.0 A cm⁻² at 2.08 V, approaching that of the precious-metal-based proton exchange membrane water electrolyser under identical conditions. In addition, the local alkalinity alleviates the degradation of non-noble metal catalysts and membrane, thus enabling the electrolyser to realise long-term stability of ~ 1400 h at 1.0 A cm⁻². We also demonstrate that this local alkalinity strategy can be readily extended to different types of membranes and scaled up, providing a universal tactic to boost the performance of anion exchange membrane water electrolyzers.

Powered by renewable electricity, proton exchange membrane water electrolyzers (PEMWEs) that can produce high-purity H₂ directly from pure water are currently the leading technology for sustainable H₂ production^{1–5}. Nevertheless, PEMWEs rely on precious-metal-based catalysts (IrO₂ and Pt), and their large-scale future deployment would considerably increase capital expenditures and the consumption of precious metals^{6,7}. Assuming a global H₂ supply of 400 GW per year, the annual demand for Ir would reach ~126 t—far exceeding its annual production (~1 t)^{5–7}. Recently, anion-exchange membrane water electrolyzers (AEMWEs)^{8–15} have attracted intensive attentions, as they eliminate the need for precious metals while retaining key advantages similar to PEMWEs.

Despite significant progress, the current performance of AEMWEs still lags far behind that of PEMWEs^{3,5}. Specifically, the hydrogen

production current density of AEMWEs supplied with pure water typically ranges 0.2–0.8 A cm⁻² at 2.0 V^{16–22}, lower than that of PEMWEs (2.0–3.0 A cm⁻² at 2.0 V)^{23–25}. The main challenge lies in the low ion conductivity of hydroxyl anions (OH⁻) in commercial anion membranes (10⁻³–10⁻² S cm⁻¹), compared to that of proton (H⁺) in PEMs (>10⁻¹ S cm⁻¹)^{10–12,26–28}. Consequently, OH⁻ generated at the cathode (2H₂O + 2e⁻ → H₂ + 2OH⁻) cannot be rapidly transported through the AEM to the anode for the oxygen evolution reaction (OER)^{20,21,26}, slowing the reaction kinetics at both electrodes. More critically, insufficient OH⁻ supply leads to anodic acidification, further degrading the long-term durability of AEMWEs (<200 h)^{17,18,22}.

To tackle the challenges posed by inefficient OH⁻ transport in AEMs, research efforts have focused on modifying the functional groups and/or backbone structures of AEM/ionomer to enhance OH⁻

¹Institute of Atomic Manufacturing, Beihang University, Beijing, China. ²School of Materials Science and Engineering, Tianjin University, Tianjin, China.

³Department of Economics, University of New Mexico, Albuquerque, NM, USA. ⁴School of Materials, Sun Yat-sen University, Shenzhen, China. ⁵Department of Applied Physics, The Hong Kong Polytechnic University, Kowloon, China. ⁶These authors contributed equally: Jiixin Guo, Ruguang Wang.

✉ e-mail: yutingyang@unm.edu; pancaofeng@buaa.edu.cn; lingt04@tju.edu.cn

conduction^{10,29–34}. While significant advancement has been achieved, improvements in OH⁻ conductivity are usually accompanied by increased water uptake and membrane swelling^{9–11,35}, which severely compromise the durability of AEMWEs. Therefore, the fundamental issue of inadequate OH⁻ transport remains unresolved, leading to sluggish reaction kinetics at both electrodes and high overpotentials in AEMWE. To mitigate these limitations, most reported AEMWE studies still employ alkaline electrolytes instead of pure water^{36–45}. However, this approach introduces critical issues, including bipolar plate passivation by alkali and the need for circulation/recovery of corrosive electrolytes^{3,9}. These issues not only raise maintenance costs but also generate substantial environmental concerns. Therefore, developing strategies to overcome the current AEMWE limitations caused by inadequate OH⁻ transport remains imperative.

In this work, we overcome the performance and stability limitations of AEMWEs by introducing titanium dioxide (TiO₂) to regulate the local microenvironment pH at both anode and cathode catalyst layers, establishing optimal alkaline conditions. Using a pH

microelectrode coupled with scanning electrochemical microscopy (SECM), we precisely monitor in situ pH distributions in the catalyst layers. Our results show that TiO₂ generates localised alkalinity within 5 μm from the catalyst surface, simultaneously enhancing reaction kinetics and OH⁻ transport. Crucially, this alkaline microenvironment effectively stabilises non-precious metal catalysts and the AEM, leading to improved AEMWE durability.

Results

Identifying the performance bottleneck of AEMWE supplied with pure water

We assembled a typical AEMWE using NiFe oxide and NiMo alloy as the anode and cathode catalysts (Supplementary Figs. 1–3), respectively, and commercial Sustainion membrane as the AEM. As shown in Fig. 1a, the AEMWE demonstrates poor performance when supplied with deionized (DI) water (hereafter, AEMWE was supplied with DI water unless otherwise specified). Electrochemical impedance spectroscopy (EIS) reveals both high ohmic resistance (R_s) and charge transfer

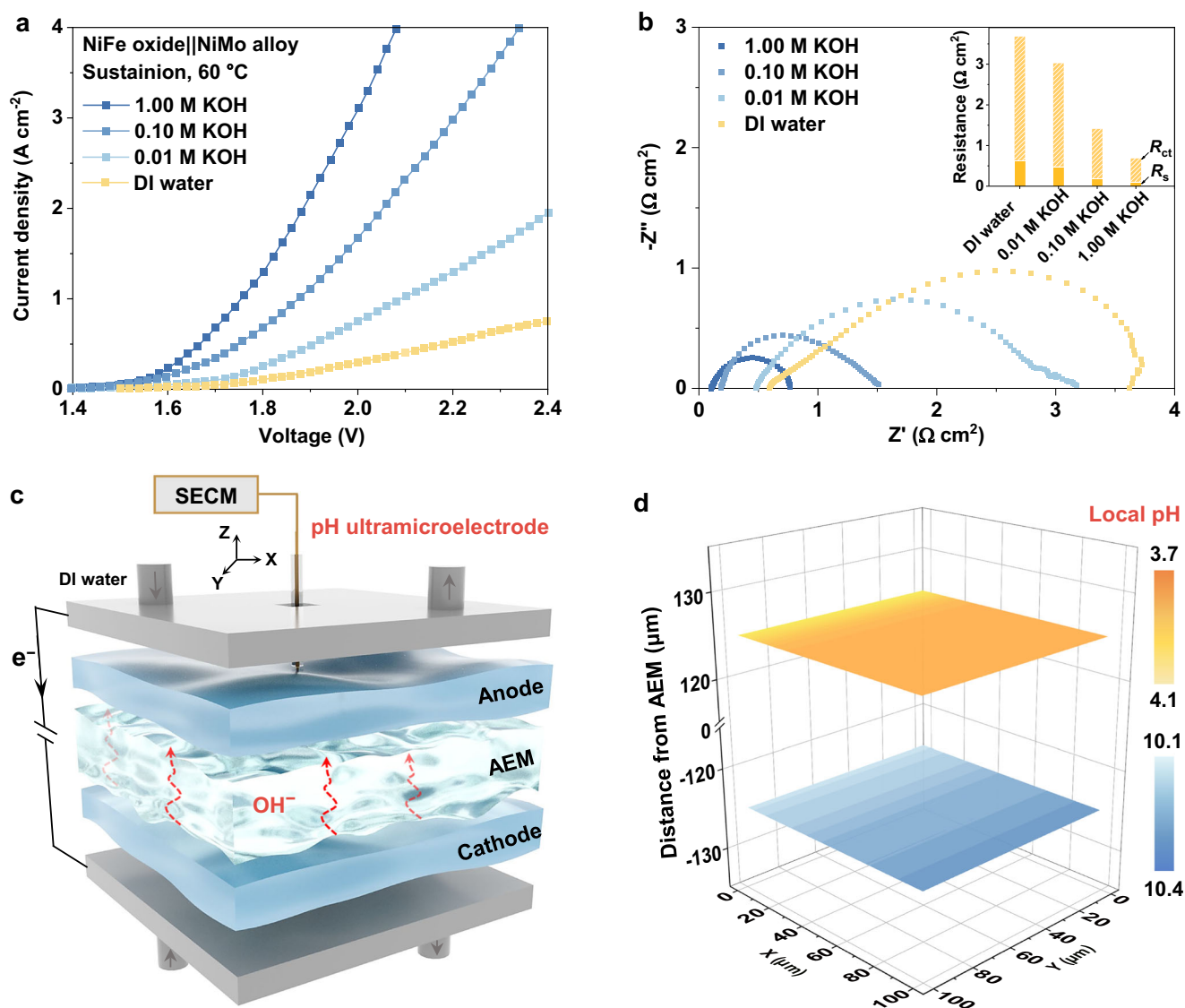


Fig. 1 | Performance and pH distributions of AEMWEs. **a** Polarisation curves of AEMWE supplied with DI water and electrolytes with different KOH concentrations. The presented voltages are not iR -corrected. **b** EIS curves of AEMWEs measured at 1.5 V, with the inset showing their R_s and R_{ct} values. **c** Schematic diagram of coupling a pH ultra-microelectrode with a SECM to monitor the in situ pH distributions

in an AEMWE. **d** Measured two-dimensional pH distribution across 3884 points within the anode and cathode catalyst layers of the AEMWE supplied with DI water. Note that the electrolyser was operated at a cell voltage of 1.9 V. Source data for Fig. 1a, b, d are provided as a Source Data file.

resistance (R_{ct}) (Fig. 1b, inset), corresponding to inefficient OH^- transport and sluggish reaction kinetics^{21,46}, respectively. Notably, adding KOH to the feed water reduces both R_s and R_{ct} values (Fig. 1b), consequently increasing the hydrogen production current density (Fig. 1a).

To investigate the reaction microenvironment of the AEMWE, we integrated a pH microelectrode ($\sim 10\ \mu\text{m}$ tip) with SECM to monitor the in situ pH distributions in the cathode and anode catalyst layers (Fig. 1c, Supplementary Note 1 and Supplementary Fig. 4). This system operates with the microelectrode measuring local pH in the AEMWE through bipolar plate openings while SECM controls its precise positioning. As illustrated in Fig. 1d, at 1.9 V cell voltage, the local pH values in the anode (pH_{anode}) and cathode catalyst layers ($\text{pH}_{\text{cathode}}$) are 3.7–4.1 and 10.1–10.4, respectively. Similar results were also found in AEMWEs with different catalyst layer thicknesses (Supplementary Figs. 5–7), confirming weakly acidic (anode) and weakly alkaline (cathode) microenvironments—a deviation from the ideal strongly alkaline conditions required for efficient operation of AEMWE. This phenomenon arises from the low OH^- conductivity of AEM— OH^- produced at the cathode cannot be rapidly transported to the anode through the membrane^{20,21,26}, which slows reaction kinetics and increasing the local pH_{anode} . In this case, the anode proceeds OER via $2\text{H}_2\text{O} \rightarrow \text{O}_2 + 4\text{H}^+ + 4\text{e}^-$, causing acidification. Notably, AEMWE supplied with 1.0 M KOH maintains pH_{anode} and $\text{pH}_{\text{cathode}}$ values of ~ 14 (Supplementary Fig. 8). These collective results demonstrate that the poor performance of AEMWE operated in DI water (Fig. 1a, b) stems from non-ideal pH conditions. Moreover, the anodic acidification further compromises the stability of the AEMWE, which will be discussed in detail later.

Creating alkaline microenvironments for both electrodes

To overcome the fundamental performance limitations of AEMWEs caused by non-ideal pH conditions, we developed a microenvironment pH-regulating strategy for both electrodes—a previously unexplored approach in AEMWEs. According to our previous work⁴⁷, the introduction of Cr_2O_3 (Cr^{3+} , $\text{p}K_a: \sim 2.05$ ⁴⁸) on a cobalt oxide catalyst can dynamically split natural seawater ($\text{pH} \sim 7.9$) and enrich OH^- near the catalyst surface. Here, we employed TiO_2 to regulate local pH in AEMWEs (Supplementary Figs. 9–11, and Supplementary Note 2), as it combines: (i) electrochemical stability across full HER and OER potential windows^{49,50}, and (ii) optimal OH^- affinity (Ti^{4+} , $\text{p}K_a: 2.20$ ⁵¹). Based on these properties, we deposited $\sim 5\ \text{nm}$ TiO_2 nanoparticles onto pre-synthesised anode NiFe oxide (anode) and NiMo alloy (cathode) catalysts (Fig. 2a, b and Supplementary Figs. 12–15).

We then assembled AEMWEs using TiO_2 -modified anode/cathode catalysts and commercial Sustainion membranes (Supplementary Tables 1, 2 and Supplementary Fig. 16). These electrolyzers, designated as TiO_2 -modified AEMWE- x (where a larger x represents an increasing TiO_2 loading), were subjected to local pH_{anode} and $\text{pH}_{\text{cathode}}$ monitoring. As illustrated in Fig. 2c, d, when no cell voltage was applied, the pH_{anode} and $\text{pH}_{\text{cathode}}$ of these TiO_2 -modified AEMWEs are both ~ 7.0 , the same as that of DI water. As the voltage increases, the pH_{anode} and $\text{pH}_{\text{cathode}}$ values increase. Moreover, when the electrolyzers were operating under the same voltage, the greater the coating amount of TiO_2 , the higher the pH_{anode} and $\text{pH}_{\text{cathode}}$ values (Fig. 2c, d and Supplementary Fig. 16). Additionally, the pH_{anode} and $\text{pH}_{\text{cathode}}$ of the TiO_2 -modified AEMWE-3 approach 14.0 when the cell voltage is $>1.55\ \text{V}$ (Fig. 2c, d; Supplementary Figs. 16 and 17), demonstrating that strong alkalinity was generated around both the anode and cathode catalyst layers. This important finding is further supported by the measured two-dimensional uniform distribution of pH_{anode} and $\text{pH}_{\text{cathode}}$ (~ 14) in this TiO_2 -modified AEMWE-3 at 1.90 V (Fig. 2e).

Moreover, we quantified the regions where the local alkalinity acts on the surface of the anode and cathode catalyst layers. Specifically, we varied the distance between the pH microelectrode and the catalyst

surface, and measured the local pH_{anode} and $\text{pH}_{\text{cathode}}$ of TiO_2 -modified AEMWE-3. As shown in Fig. 2f, when the distance between the two is less than $5\ \mu\text{m}$, the measured pH_{anode} ranges 13.8–12.9, and this value rapidly drops to ~ 7.0 when the distance exceeds $5\ \mu\text{m}$. For $\text{pH}_{\text{cathode}}$, a similar trend was observed (Fig. 2g). These results indicate that the local strong alkalinity is in the range of $5\ \mu\text{m}$ on the anode and cathode catalyst surface.

Mechanism of TiO_2 -mediated OH^- enrichment

To elucidate the formation mechanism of local alkalinity in AEMWEs, in situ surface-enhanced Raman spectroscopy was employed (Fig. 3). For the anode in a neutral electrolyte, TiO_2 (Fig. 3a) and TiO_2 -modified NiFe oxide (Fig. 3c; Supplementary Figs. 18 and 19) exhibit potential-dependent enhancement of the H–O–H bending vibration ($\sim 1600\ \text{cm}^{-1}$) from adsorbed water (H_2O^*)⁵², accompanied by emerging OH^* peaks ($\sim 800\ \text{cm}^{-1}$)^{52,53}. This indicates active water dissociation on TiO_2 (Supplementary Note 3 and Supplementary Fig. 20), in sharp contrast to pristine NiFe oxide under the same conditions (Fig. 3b), which shows negligible H_2O^* and OH^* signals. Obviously, the potential-dependent evolution of these spectral features shows a clear correlation with the pH_{anode} measurements (Fig. 2c), where TiO_2 -modified AEMWEs exhibit evident OH^- accumulation (and thus increased pH_{anode}), while the pristine AEMWE shows negligible change. This direct correspondence provides spectroscopic evidence that the local alkalinity originates from accelerated water dissociation on TiO_2 ($\text{H}_2\text{O} \rightarrow \text{OH}^- + \text{H}^+$). Our density functional theory calculations support this point, revealing that TiO_2 exhibits a low energy barrier for water dissociation under anode potential (Supplementary Fig. 21). This facilitated dissociation leads to the accumulation of OH^- within the electrical double layer (EDL) due to electrostatic attraction to the positively charged electrode surface (Supplementary Fig. 22), while the generated H^+ is rapidly extracted from the EDL under the applied potential gradient (Fig. 3e). This selective ion redistribution creates an alkaline microenvironment at the anode interface.

At the cathode, while the pristine TiO_2 and NiMo alloy in neutral electrolyte (Fig. 3f, g) show weak H_2O^* signals, TiO_2 -modified NiMo alloy exhibits enhanced H_2O^* intensity and rapidly increasing H^* signals ($\sim 1950\ \text{cm}^{-1}$)²⁴ with applied potential (Fig. 3h and Supplementary Fig. 23). These observations clearly demonstrate that the local alkalinity at the cathode (Fig. 2d) develops through a mechanism distinct from the anode's direct water dissociation on TiO_2 . This should be a synergistic mechanism between TiO_2 and NiMo alloy (Fig. 3e), where the NiMo alloy catalyzes the Volmer step of HER ($\text{H}_2\text{O} + \text{e}^- \rightarrow \text{OH}^- + \text{H}^*$)⁵⁴, while oxophilic TiO_2 ^{50,55} adsorbs and enriches OH^- . This OH^- feedback accelerates the Volmer step on NiMo alloy, thereby establishing a self-sustaining alkaline microenvironment.

The above results demonstrate that at both electrodes, TiO_2 enriches OH^- in the EDL. The resulting alkaline environments enable the anode NiFe oxide and cathode NiMo alloy catalysts to proceed via alkaline OER and HER mechanisms, respectively. This is evidenced by the pronounced O–O bond⁵³ (Supplementary Fig. 24) and H^* intermediates observed on the TiO_2 -modified NiFe oxide and NiMo in neutral electrolyte (Fig. 3c, h), similar to their behaviour in the alkaline electrolyte (Fig. 3d, i; Supplementary Note 4; Supplementary Figs. 25 and 26). Undoubtedly, this effect can enhance the reaction kinetics at both electrodes.

Performance of locally alkaline AEMWE

As discussed above, the performance of the pristine AEMWE is limited by unfavourable OH^- transport and sluggish reaction kinetics (high R_s and R_{ct} , Fig. 1b). EIS measurements show that the R_s and R_{ct} values of the locally alkaline AEMWE (TiO_2 -modified AEMWE-3) are reduced compared to those of the pristine AEMWE (Fig. 4a). Moreover, it is found that the local alkalinity can also improve the OH^- conductivity of AEM in DI water, with its value close to that of the membrane in 1.0 M

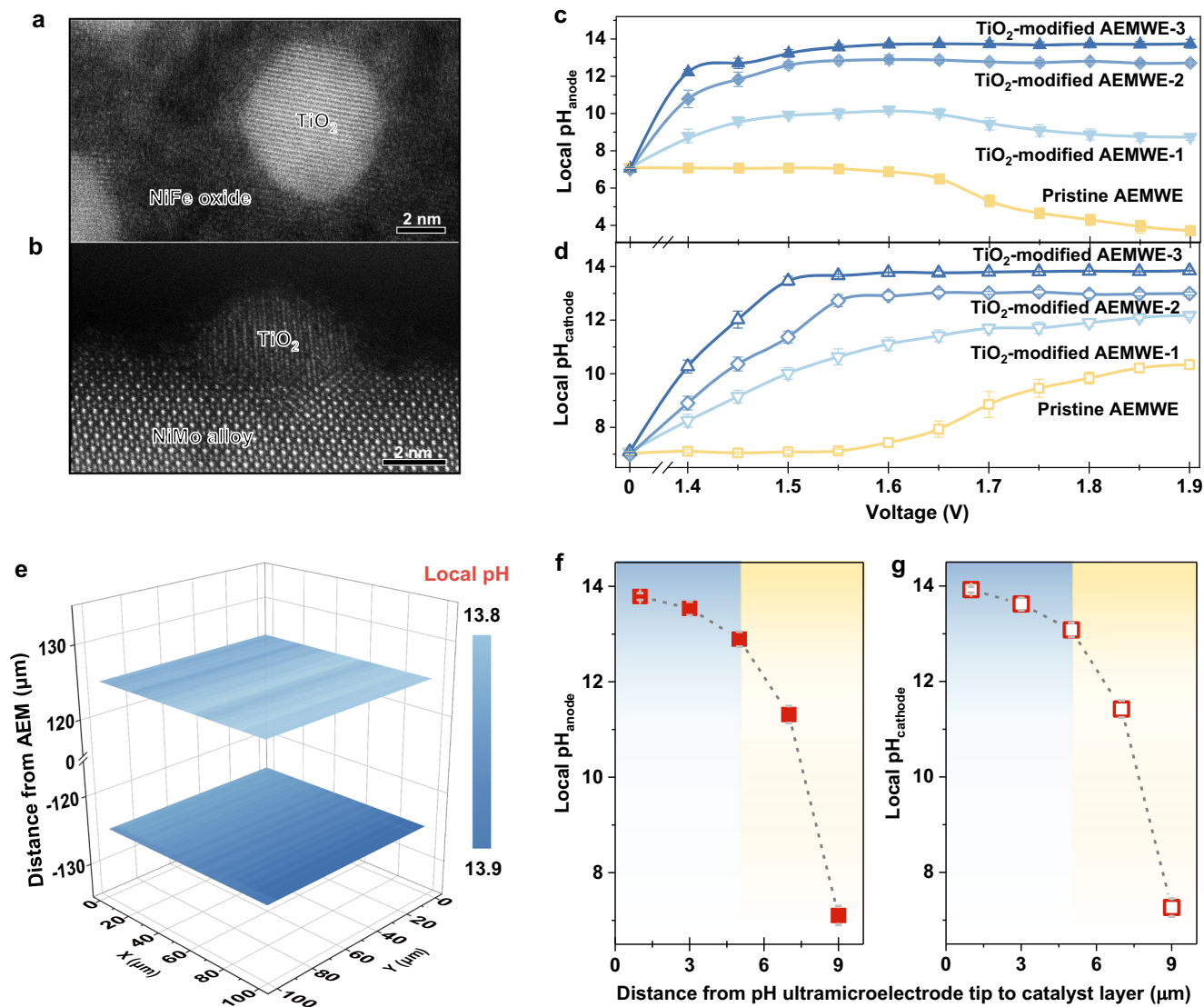


Fig. 2 | Monitoring in situ pH distributions in TiO₂-modified AEMWEs.

a, b Atomic-scale high-angle annular dark-field (HAADF) images of TiO₂-modified NiFe oxide and NiMo alloy, respectively. **c, d** Local pH_{anode} and pH_{cathode} of the TiO₂-modified AEMWEs under varied cell voltages, respectively. **e** Two-dimensional pH distributions within the anode and cathode catalyst layers of the TiO₂-modified AEMWE-3 at a cell voltage of 1.9 V. **f** Relationship between local pH_{anode} and

distance from the pH ultra-microelectrode tip to the anode catalyst layer.

g Corresponding relationship for the cathode catalyst layer. Note that the local pH values in **(c, d, f, g)** were averaged over measurements taken at three distinct points, and the standard deviations were marked by the error bars. Source data for Fig. 2c–g are provided as a Source Data file.

KOH (Fig. 4b and Supplementary Fig. 27). This finding is reasonable that due to the boosted hydrogen evolution kinetics, a large amount of OH⁻ is produced ($2\text{H}_2\text{O} + 2\text{e}^- \rightarrow \text{H}_2 + 2\text{OH}^-$), which increases the occupancy and transport of OH⁻ in the membrane. Therefore, the local alkalinity can solve the critical issues of inefficient OH⁻ transport and sluggish reaction kinetics in AEMWEs.

As a result, the locally alkaline AEMWE delivers a high hydrogen generation current density of 3.0 A cm^{-2} at 2.08 V, which is 8 times that of the pristine AEMWE (Fig. 4c; Supplementary Figs. 28 and 29). This performance is competitive with those reported for AEMWEs supplied with pure water^{16,17,19–21,56} and approaches that of the state-of-the-art PEMWE^{23–25} (Supplementary Table 3). It is noteworthy that the slight performance reduction of the locally alkaline AEMWE compared with that of the pristine AEMWE operated in 1.0 M KOH is due to the fact that TiO₂ covers some active sites on the anode and cathode catalysts (Supplementary Fig. 30).

We further validated this microenvironment regulation strategy in electrolysers incorporating additional commercial AEMs (AEMION™

and FAA), alongside the above investigated Sustainion membrane (Figs. 1 and 2). These membranes employ distinct OH⁻ conduction mechanisms: Sustainion uses imidazole-functionalized polystyrene, AEMION™ relies on methylated polybenzimidazole, and FAA depends on quaternary ammonium groups⁵⁷. TiO₂-modification consistently establishes local alkalinity across all membrane types (Supplementary Figs. 31 and 32), leading to performance enhancements. Specifically, at 1.9 V, the modified Sustainion-, AEMION™-, and FAA-based AEMWEs exhibit 9-, 8-, and 7-fold increases in hydrogen production current density, respectively, compared to their unmodified counterparts (Fig. 4d; Supplementary Figs. 33 and 34). This universal performance improvement across diverse membrane chemistries demonstrates the broad applicability of our microenvironment regulation strategy.

Long-term stability of locally alkaline AEMWE

Another key challenge of AEMWEs for practical applications is their poor long-term stability^{17,22,27}. As discussed above, the local reaction environment of the anode catalyst in the pristine AEMWE is weakly

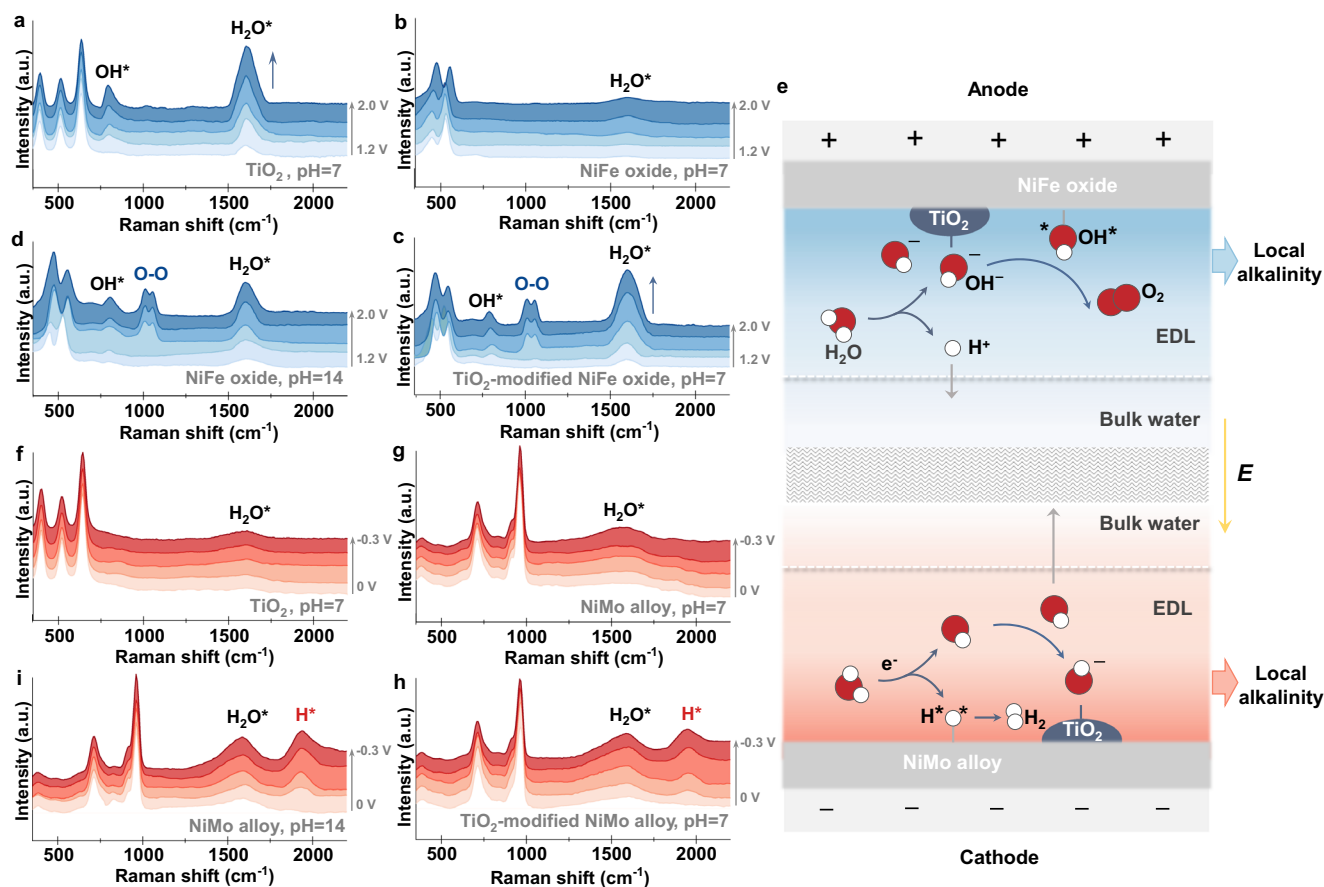


Fig. 3 | Investigating mechanism of local alkalinity. In situ surface-enhanced Raman spectra of (a) TiO₂, b NiFe oxide, c TiO₂-modified NiFe in 0.5 M Na₂SO₄ (pH - 7, 7.02 ± 0.07), and d pristine NiFe oxide in 1.0 M KOH (pH - 14, 13.93 ± 0.03), recorded at potentials ranging from 1.2 to 2.0 V (specifically at 1.2, 1.4, 1.6, 1.8 and 2.0 V) versus the reversible hydrogen electrode (V_{RHE}). e Schematic diagram of locally alkaline microenvironments generated on anode and cathode. The orange

arrow represents the direction of external electric field (E). EDL = Electric double layer. In situ surface-enhanced Raman spectra of (f) TiO₂, g NiMo alloy, h TiO₂-modified NiMo alloy in 0.5 M Na₂SO₄ (pH-7, 7.02 ± 0.07), and i pristine NiMo alloy in 1.0 M KOH (pH-14, 13.93 ± 0.03), recorded at potentials ranging from 0 to -0.3 V_{RHE} (specifically at 0, -0.05, -0.1, -0.2, and -0.3 V_{RHE}). Source data for Fig. 3a-d, f-h are provided as a Source Data file.

acidic (pH ~4.0, Fig. 1d), which can obviously cause structural degradation of non-precious metal catalysts. To clarify this point, we quantified Fe and Ni dissolution from the anode NiFe oxide catalyst after 100 h operation at 1.9 V in both the pristine and locally alkaline AEMWEs. Note that the pH_{anode} values of these AEMWEs are 3.7 (pristine), 8.7, 12.7 and 13.8 (locally alkaline) (Fig. 2c and Supplementary Fig. 35). As shown in Fig. 5a, the pristine AEMWE shows substantial metal dissolution (43 at% Fe, 59 at% Ni), confirming the destabilising effect of acidic conditions (Supplementary Fig. 36). Conversely, locally alkaline AEMWEs exhibit progressively reduced dissolution with increasing pH_{anode} . Specifically, for the AEMWE with local pH_{anode} of 13.8, the loss of Fe and Ni from the anode catalyst becomes negligible (Fig. 5a and Supplementary Fig. 36). Therefore, the in situ generated local alkalinity can effectively inhibit the detrimental dissolution of the anode catalyst.

Furthermore, according to previous works^{17,58}, the anodic acidification can lead to degradation of membranes. Therefore, we pay close attention to the effect of pH_{anode} on the structural changes of AEM after its assembly and operation in the electrolyser. Figure 5b shows the X-ray photoelectron spectroscopic (XPS) spectra of the original and used Sustainion membranes with different pH_{anode} . As illustrated, the original membrane exhibits evident N⁺ (401.5 eV) and C - N⁺ (287.0 eV) peaks⁵⁸ from its imidazole groups, which are crucial for OH⁻ conduction. Notably, as pH_{anode} decreases, the intensities of the N⁺ and C-N⁺ signals decrease, suggesting H⁺-induced degradation

of imidazole groups. Furthermore, when the membrane was operated at pH_{anode} values of 8.7 and 3.7, a O-C=O (288.4 eV) appears, indicating oxidative degradation of the polymer chain⁵⁸. In contrast, there is no noticeable change observed in the membrane of the locally alkaline AEMWE with pH_{anode} of 13.8. These results demonstrates that in situ generated local alkalinity can effectively suppress AEM degradation.

Afterwards, we evaluated the long-term stability of our locally alkaline AEMWE (TiO₂-modified AEMWE-3). As shown in Fig. 5c, this electrolyser works stably for more than 1400 h at a high current density of 1.0 A cm⁻², with a voltage drift as small as 60 $\mu\text{V h}^{-1}$. Such stability is better than those reported for AEMWEs operating in pure water^{10,16-18,22,29} (in the range of 10–200 h and measured at lower current densities of 100–500 mA cm⁻²). This finding is further supported by our measured changes in the local pH_{anode} and $\text{pH}_{\text{cathode}}$ of our locally alkaline AEMWE as a function of time (Fig. 5d, e and Supplementary Fig. 37), which demonstrated that the strong local alkalinity in the anode and cathode catalyst layers was well maintained during the operation of the electrolyser.

Scale up of locally alkaline AEMWE

We fabricated a 10-cell locally alkaline AEM stack connected in series (Fig. 6a), featuring a total electrode area of 250 cm² (25 cm² per single cell). As shown in Fig. 6b, individual cells perform similarly, obtaining a current density of 2.0 A cm⁻² at 1.94 ± 0.02 V, while the overall stack achieves the same current density at 21.0 V. Moreover, our locally

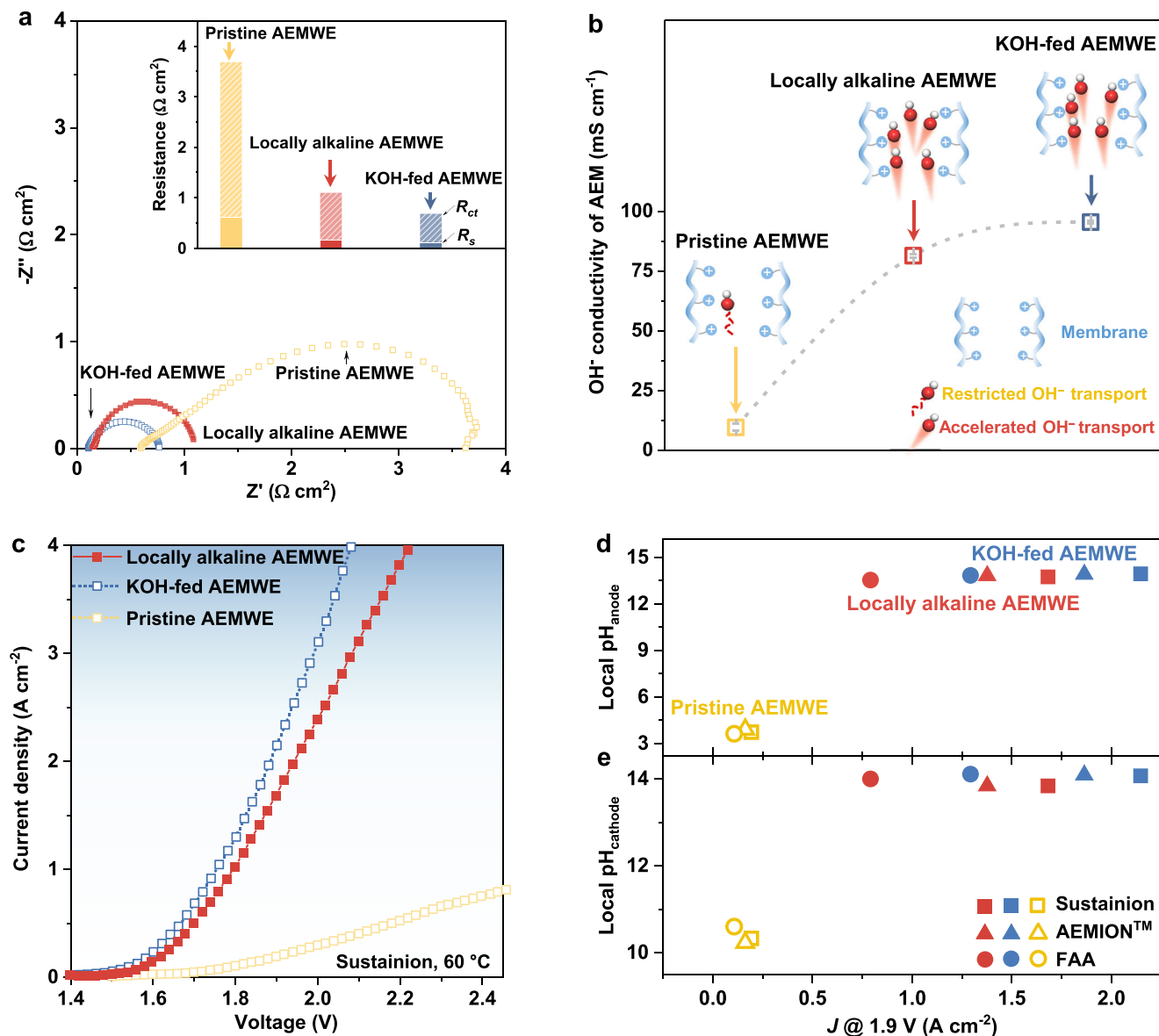


Fig. 4 | Local alkalinity enhancing performance of AEMWE. **a** EIS curves of AEMWEs operating in DI water and 1.0 M KOH, with the inset showing their corresponding R_s and R_{ct} values. Note that the locally alkaline AEMWE is TiO₂-modified AEMWE-3 and the EIS measurements were performed at a cell voltage of 1.5 V. **b** Measured OH⁻ conductivity of AEM in DI water and 1.0 M KOH. Note that the values of OH⁻ conductivity were both averaged over three repeated measurements, and the standard deviations were marked by the error bars. The inset schematic illustration shows that local alkalinity can increase the occupancy and transport of

OH⁻ in the membrane. **c** Polarisation curves of the pristine AEMWE and locally alkaline AEMWE supplied with DI water. Note that the performance of the pristine AEMWE operating in 1.0 M KOH electrolyte was added for reference. The presented voltages are not iR -corrected. **d, e** Relationship among hydrogen production current density, local pH_{anode}, and local pH_{cathode} of AEMWEs assembled with different types of AEMs. Note that the electrolyzers were operated at 1.9 V. Source data are provided as a Source Data file.

alkaline AEM stack demonstrates good durability with a degradation rate of 117 $\mu\text{V h}^{-1}$ during 500 h of operation at 1.0 A cm⁻² (Fig. 6c). Assuming maintenance of >80% initial performance at this decay rate, the projected operational lifetime of the stack exceeds 32,000 h—a duration that would satisfy industrial requirements. Importantly, the locally alkaline AEM stack supplied with DI water achieves an energy consumption of 49.5 kWh kg⁻¹ H₂ and an energy conversion efficiency of 74.5% (Fig. 6c), comparable to those of the state-of-the-art PEM stack based on precious metal catalysts (46.6 kWh kg⁻¹ H₂ and 79.2% conversion efficiency), also approaching the Department of Energy's (DOE) 2050 target for AEMWE technology (75% conversion efficiency).

To assess economic viability, we conducted a leveled cost of hydrogen (LCOH) analysis (Supplementary Note 5 and Supplementary Figs. 38–41). The results demonstrate cost advantages for our locally

alkaline AEM stack compared to precious-metal-dependent PEM systems, with a median LCOH reduction of 25.4% (Supplementary Fig. 38). When compared to KOH-enhanced AEM systems, our approach maintains competitive performance while effectively avoiding the operational challenges associated with alkaline corrosion and wastewater treatment, exhibiting economic stability (Supplementary Figs. 39–41). This combination of technical advantages and economic benefits positions our locally alkaline AEMWE technology as an ideal solution for commercial hydrogen production.

Discussion

In summary, we proposed an AEM-independent strategy to adjust the reaction microenvironment of anode and cathode catalyst layers to ideal strong alkalinity, thus effectively addressing the performance

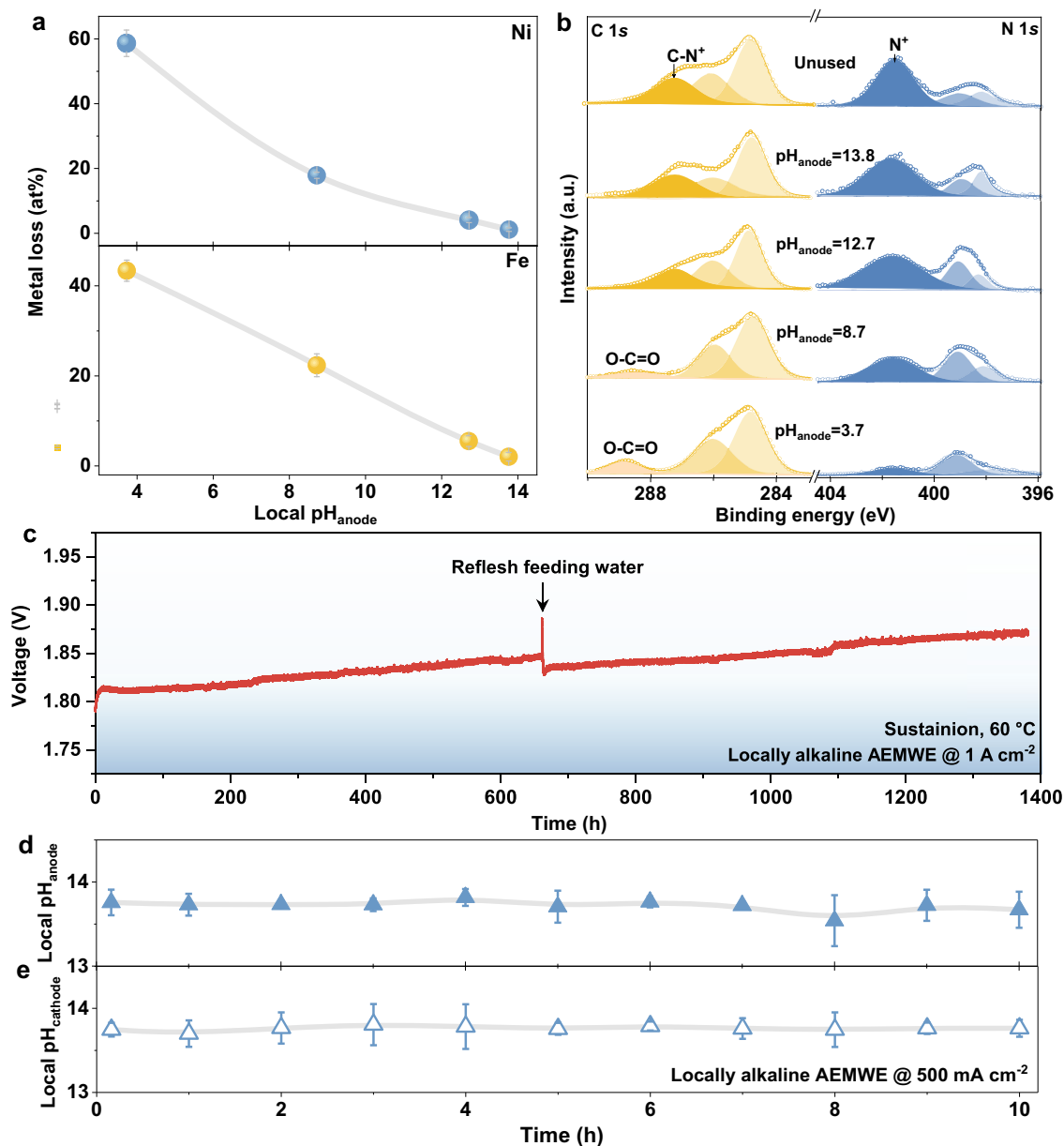


Fig. 5 | Stability of AEMWE supplied with DI water. **a** Dissolved atomic ratios of Fe and Ni atoms from the anode NiFe oxide catalysts when pH_{anode} varies. Note that the quantification of dissolved Fe and Ni atoms from the catalysts were carried out after operating the electrolyzers at 1.9 V for 100 h. **b** C 1s and N 1s XPS spectra of the original and used Sustainion membrane with varied pH_{anode} . Note that the electrolyzers were disassembled after 100 h operation at 1.9 V, then the membranes were characterized by XPS. **c** Chronopotentiometry curve of the locally alkaline AEMWE

operating at 1.0 A cm⁻². **d, e** Local pH_{anode} and $\text{pH}_{\text{cathode}}$ of locally alkaline AEMWE as a function of time, respectively. Note that the electrolyser was operated at a hydrogen current density of 500 mA cm⁻². Note that the values of local pH in **d** and **e** were both averaged over measurements taken at three distinct points, and the standard deviations were marked by the error bars. Source data are provided as a Source Data file.

limitations associated with AEMs in electrolyzers. We demonstrated that the super in situ generated local alkalinity not only boosted the hydrogen production, but also suppressed the degradation of non-noble metal catalysts and AEM. As a result, our locally alkaline AEMWE, assembled with commercial AEM and supplied with DI water, achieved a hydrogen generation current density of 3.0 A cm⁻² at 2.08 V, and exhibited stability up to 1400 h at an industrial required current density of 1.0 A cm⁻². We demonstrate that such in situ generated local alkalinity enables AEMWEs to compete with the leading PEMWEs. Moreover, our specifically engineered AEM stack contributes to lower capital expenditures and maintenance costs, minimised alkali waste treatment demands, and paves the way for the industrial application of AEMWE electrolysis technology.

Methods

Materials synthesis

The NiFe oxide catalyst was fabricated by a solvothermal method. Specifically, a precursor solution was firstly prepared by dissolving 0.5 mM Ni(NO₃)₂·6H₂O (≥99%, Aladdin), 0.5 mM Fe(NO₃)₃·9H₂O (≥99%, Aladdin) and 10 mM urea (≥99%, Aladdin) in 35 mL of DI water. Then, a pre-cleaned Ni fibre felt was placed vertically in the precursor solution, transferred to a 50 mL Teflon autoclave and treated at 120 °C for 12 h. Afterwards, the Ni fibre felt was thoroughly washed with DI water, dried at room temperature (25 °C), and heated in N₂ atmosphere at 600 °C for 2 h to obtain the NiFe oxide catalyst. Note that the loading mass of as-prepared NiFe oxide catalyst on Ni fibre felt was ~3 mg cm⁻².

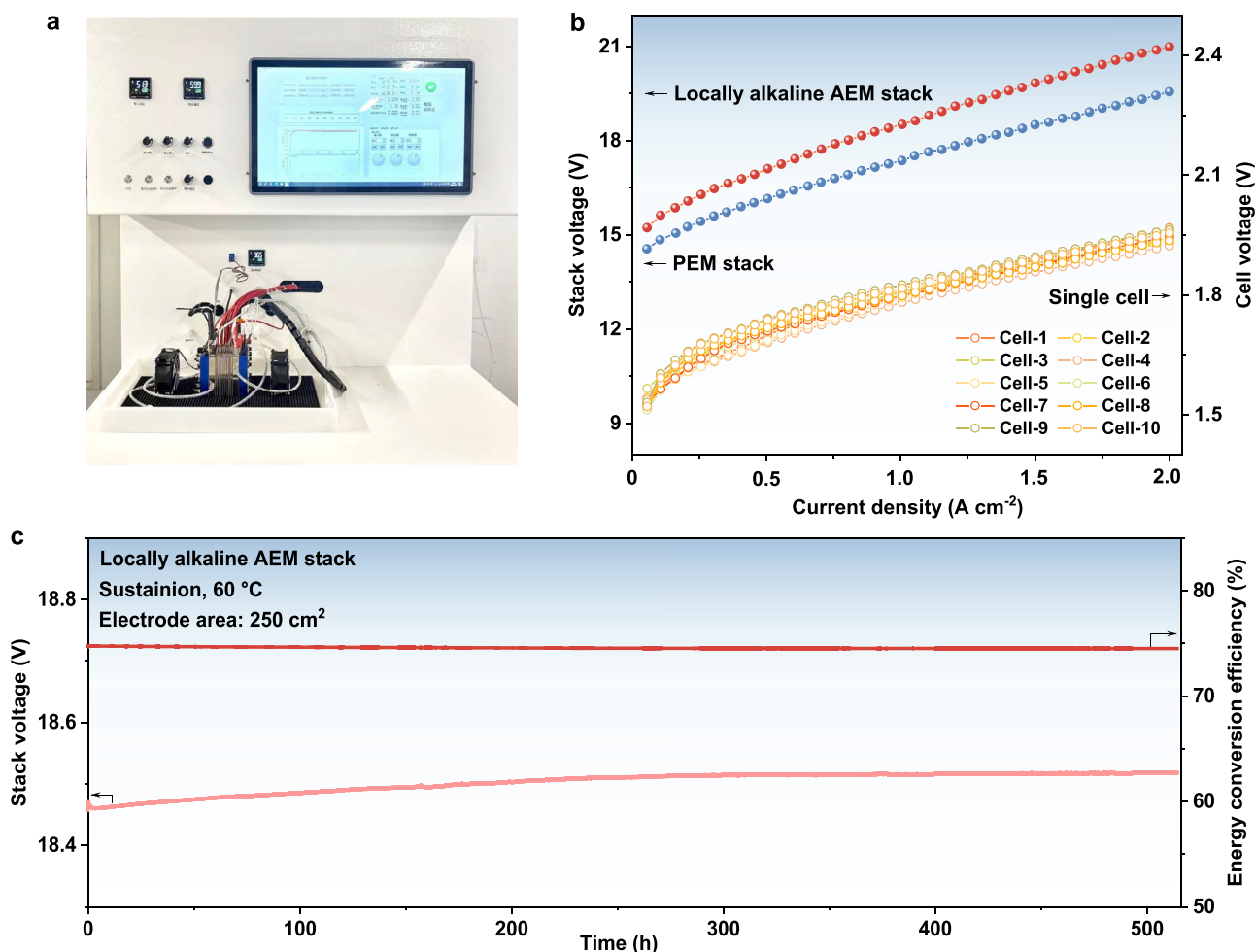


Fig. 6 | Scale up for locally alkaline AEMWE. **a** Digital picture of the 10-cell AEM stack using Sustainion membrane. **b** Polarisation curves of the AEM stack and each cell supplied with DI water. Note that the curve of the PEM stack is added for

reference. The presented voltages are not *iR*-corrected. **c** Durability test and energy conversion efficiency of the AEM stack supplied with DI water at 1.0 A cm⁻². Source data for Fig. 6b, c are provided as a Source Data file.

The NiMo alloy catalyst was synthesised according to the previous work⁵⁴. Firstly, a precursor solution was prepared by dissolving 0.08 M Ni(NO₃)₂·6H₂O and 0.02 M (NH₄)₆Mo₇O₂₄·4H₂O (99%, Aladdin) in 30 mL of deionized water. Afterwards, a pre-cleaned Ni fibre felt was placed in the precursor solution, then transferred to a 50 mL Teflon autoclave, and treated at 150 °C for 6 h. Next, the Ni fibre felt was washed with DI water, dried naturally and reduced at 600 °C for 2 h under H₂/Ar (v/v = 15/85) atmosphere to obtain NiMo alloy catalyst. Note that the loading mass of NiMo alloy catalyst on Ni fibre felt was ~3.2 mg cm⁻².

For the TiO₂-modified NiFe oxide or NiMo alloy catalysts, a titanium precursor was prepared by dissolving titanium isopropyl alcohol (TiC₉H₁₉NO₄) in ethanol. Then, the Ni fibre felt loaded with NiFe oxide or NiMo alloy catalyst was immersed in the precursor solution, dried naturally and heated at 400 °C for 3 h in N₂ flow to obtain the TiO₂-modified NiFe oxide or NiMo alloy catalyst. Note that for 4, 8, 12 and 20 at% TiO₂-modified NiFe oxide, 0.05, 0.1, 0.2, 0.5 M TiC₉H₁₉NO₄ in ethanol were used as precursor, respectively. For 2, 7, 10 and 16 at% TiO₂-modified NiMo alloy, 0.02, 0.1, 0.2, 0.5 M TiC₉H₁₉NO₄ in ethanol were used, respectively.

Materials characterisation

Scanning electron microscopy (SEM) and transmission electron microscopy (TEM) images were carried out on a Hitachi S-4800 SEM

and a JOEL 2100 TEM, respectively. X-ray diffraction patterns (XRD) were obtained using a Bruker D8 Advance diffractometer with a Cu K α radiation operating at 20 kV. Inductively coupled plasma mass spectrometry (ICP-MS) measurements were performed on an Agilent Varian 700. XPS spectra were collected using a K α Thermo Fisher spectrometer. Local pH measurements were carried out on a commercial CHI920D SECM system (CH Instruments, China), which was placed on a shock-proof platform to minimise vibration disturbance. The whole testing system was put in a shielding box. The performance of AEMWEs was measured using a programmable DC power supply (ITECH).

In situ surface-enhanced Raman spectroscopy

In situ surface-enhanced Raman spectra were collected using a confocal Raman microscope (Horiba LabRAM HR Evolution) equipped with an excitation wavelength of 532 nm and a 50 \times objective (Supplementary Fig. 18). Each Raman spectrum was acquired over a collection time of 30 s and was the average of three measurements. The working electrode was a rough Au electrode loaded with catalyst. The counter electrode was a Pt wire and the reference electrode was Ag/AgCl/KCl (3.0 M). The latter was calibrated in H₂-saturated electrolyte using Pt foils as both counter and working electrodes. All OER and HER potentials were converted to the RHE scale by averaging the two zero-current potentials from cyclic voltammetry scans at 1 mV s⁻¹. The

conversion used was $V_{\text{RHE}} = V_{\text{Ag/AgCl}} + 0.61 \text{ V}$ in 0.5 M Na_2SO_4 and $V_{\text{RHE}} = V_{\text{Ag/AgCl}} + 1.02 \text{ V}$ in 1.0 M KOH. In addition, laser irradiation was performed for 1 h before in situ test.

Measurement of local pH distributions in catalyst layers of AEMWE

The Pt/IrO₂ microelectrode was fabricated based on electrochemical cyclic voltammetry⁵⁹. First, the iridium precursor solution for electrodeposition was prepared. Specifically, 0.075 g of $\text{IrCl}_4 \cdot x\text{H}_2\text{O}$ (99.99%, Alfa Aesar) was dissolved in 50 mL of pure water and magnetically stirred for 30 min. Subsequently, 0.5 mL of H₂O₂ (30 wt%, Merger) was added, and the mixture was further stirred magnetically for an additional 10 min. Then, 0.25 g of oxalic acid (99.5%, Merger) was introduced, followed by continued stirring for another 10 min. Anhydrous potassium carbonate was gradually added to adjust the pH to 10.5. The resulting solution was stirred for 2 days, during which it gradually turned dark blue, and then stored at 25 °C for subsequent use. The electrodeposition experiments were conducted in a three-electrode configuration using the prepared iridium solution, with a 10 μm diameter Pt microelectrode serving as the working electrode, a Pt wire as the counter electrode, and an Ag/AgCl/KCl (3.0 M) electrode as the reference electrode. Cyclic voltammetry was carried out over a potential range of 0.2 to 0.75 V (vs. Ag/AgCl) at a scan rate of 50 mV s⁻¹ for 100 cycles in the previously prepared Ir iridium solution. After electrodeposition, the Pt/IrO₂ microelectrode was removed, rinsed with pure water, dried, and then aged in an oven at 100 °C for 2 h before being stored for further use.

To measure the local pH within AEMWEs, a three-electrode configuration was established using a Pt/IrO₂ microelectrode as the working electrode, a Pt wire and an Ag/AgCl electrode as the counter electrode and reference electrode, respectively. Furthermore, precise movement of the Pt/IrO₂ microelectrode was realised by the controlling of SECM. For measuring the pH within the catalyst layers, an area of 1 × 1 cm² was opened in the bipolar plate of the AEMWE (Fig. 1c). During the test, the Pt/IrO₂ microelectrode approached the catalyst layer at a rate of 0.2 μm s⁻¹, and the open circuit potential (E_{oc}) was monitored. Once the tip of the Pt/IrO₂ microelectrode contacted the catalyst layer, a marked change in E_{oc} was observed (Supplementary Fig. 4), and the Pt/IrO₂ microelectrode was subsequently lifted upward at a rate of 0.2 μm s⁻¹. When the tip was 1.0 μm away from the catalyst layer, E_{oc} was recorded, and the corresponding local pH value in the catalyst layer was deduced based on its relationship with E_{oc} (Supplementary Fig. 4), as shown detailed in the previous works^{47,59}. The two-dimensional pH distribution with dimensions of 100 × 100 μm² was mapped at a scan rate of 40 μm s⁻¹. All measurements were performed for at least three repetitions.

Membrane electrode assembly (MEA)

For the AEMWE, commercial anion-exchange membranes (Sustainion X37-50, AEMION™ AF1-HNN8-50-X, or FAA-3-50; thickness: 50 μm) were employed. Each membrane was pre-treated with 1.0 M KOH for 48 h, and then treated with fresh KOH for 24 h. Next, the membrane was washed with DI water until the pH of the water reached neutral. The catalyst integration comprised two components: pre-grown catalysts directly on nickel fibres and catalysts spray-coated onto the membrane. For the spray-coated catalysts, NiFe oxide and NiMo alloy were first exfoliated from nickel felt substrates via ultrasonication. Catalyst inks were prepared by homogeneously dispersing 100 mg of the exfoliated catalysts in 10 mL of isopropanol/water mixture (9:1, v/v) with 10 wt% Sustainion XB-7 ionomer (relative to catalyst mass) under 3 h sonication. These inks were then deposited onto both sides of the pretreated AEM using ultrasonic spray coating, achieving a loading of approximately 1 mg cm⁻². Then, the spray-coated AEM, the Ni fibres loaded with NiFe oxide (-3.0 mg cm⁻²) and NiMo alloy (-3.2 mg cm⁻²)

catalysts, and Teflon gaskets were assembled together with a torque wrench tighten the screws to 5.0 N m⁻¹ (Supplementary Fig. 1).

For each cell of the PEM stack, a Nafion 115 membrane was utilised and subjected to sequential 1-hour treatments at 80 °C in 5 wt% H₂O₂, 1.0 M H₂SO₄, and DI water. Then, the membrane was rinsed with DI water until neutral pH was achieved. Following this, commercial IrO₂ (2.0 mg cm⁻²) and Pt/C (0.5 mg_{Pt} cm⁻²) catalysts were sprayed onto both sides of the prepared PEM. For catalyst inks (Pt/C and RuO₂) ink preparation, 100 mg of catalyst (Pt/C or RuO₂) was ultrasonically dispersed for 2 h at 25 °C in a 10 mL mixture of isopropanol and water (1:3 v/v) containing 5 wt% Nafion. The assembly was completed by stacking the catalyst-coated membrane with Ti fibre felts and Teflon gaskets, and tightening the screws to a torque of 5.0 N m⁻¹ with a torque wrench.

Electrolyser and stack tests

During tests, the feed water/electrolyte was continuously supplied to both electrodes of the AEM electrolyser (active area: 1 × 1 cm²) and 10-cell stack (single cell active area: 5 × 5 cm²) using a two-channel peristaltic pump, with flow rates maintained at 20 mL/min for the electrolyser and 200 mL/min for the stack (Supplementary Note 6). The operating temperature of the electrolyser was maintained at 60 °C using a temperature controller and thermocouples integrated into the endplates. Note that the electrolytes used were pure water (pH = 7.04 ± 0.08) or 1.0 M KOH (pH = 13.93 ± 0.03), both solutions were freshly prepared before each test. Prior to testing, the electrolyser (or stack) underwent a pre-activation procedure via chronopotentiometry, with the current density stepped from 0.1 to 1.0 A cm⁻² (increments of 0.1 A cm⁻², 1 min per step)²⁴. Polarisation curves without iR compensation were then recorded by stepping the voltage from 1.4 to 2.4 V (increments of 0.02 V, 20 s per step). EIS was subsequently conducted at 1.5 V, with a frequency range from 100 kHz to 0.01 Hz and an amplitude of 5 mV.

Data availability

The data that support the findings of this study are available within this article and its Supporting Information. Source data are provided with this paper.

References

1. Chu, S. & Majumdar, A. Opportunities and challenges for a sustainable energy future. *Nature* **488**, 294–303 (2012).
2. Kibsgaard, J. & Chorkendorff, I. Considerations for the scaling-up of water splitting catalysts. *Nat. Energy* **4**, 430–433 (2019).
3. Lagadec, M. & Grimaud, A. Water electrolyzers with closed and open electrochemical systems. *Nat. Mater.* **19**, 1140–1150 (2020).
4. Liu, R. T. et al. Recent advances in proton exchange membrane water electrolysis. *Chem. Soc. Rev.* **52**, 5652–5683 (2023).
5. *Scaling up electrolyzers to meet the 1.5°C climate goal*; <https://www.irena.org/publications/2020/Dec/Green-hydrogen-cost-reduction> (IRENA, 2020).
6. Hubert, M. A., King, L. A. & Jaramillo, T. F. Evaluating the case for reduced precious metal catalysts in proton exchange membrane electrolyzers. *ACS Energy Lett.* **7**, 17–23 (2021).
7. Minke, C., Suermann, M., Bensmann, B. & Hanke-Rauschenbach, R. Is iridium demand a potential bottleneck in the realization of large-scale PEM water electrolysis? *Int. J. Hydrog. Energy* **46**, 23581–23590 (2021).
8. Yang, Y. et al. Anion-exchange membrane water electrolyzers and fuel cells. *Chem. Soc. Rev.* **51**, 9620–9693 (2022).
9. Du, N. et al. Anion-exchange membrane water electrolyzers. *Chem. Rev.* **122**, 11830–11895 (2022).
10. Li, D. et al. Highly quaternized polystyrene ionomers for high performance anion exchange membrane water electrolyzers. *Nat. Energy* **5**, 378–385 (2020).

11. Mardle, P., Chen, B. & Holdcroft, S. Opportunities of ionomer development for anion-exchange membrane water electrolysis. *ACS Energy Lett.* **8**, 3330–3342 (2023).
12. Hu, X. et al. An operationally broadened alkaline water electrolyser enabled by highly stable poly(oxindole biphenylene) ion-solvating membranes. *Nat. Energy* **9**, 401–410 (2024).
13. Abbasi, R. et al. A roadmap to low-cost hydrogen with hydroxide exchange membrane electrolyzers. *Adv. Mater.* **31**, 1805876 (2019).
14. Lohmann-Richters, F. P., Renz, S., Lehnert, W., Müller, M. & Carmo, M. Review—Challenges and opportunities for increased current density in alkaline electrolysis by increasing the operating temperature. *J. Electrochem. Soc.* **168**, 114501 (2021).
15. Zhai, T. et al. Perovskite catalysts for pure-water-fed anion-exchange-membrane electrolyzer anodes: co-design of electrically conductive nanoparticle cores and active surfaces. *J. Am. Chem. Soc.* **147**, 15448–15458 (2025).
16. Razmjooei, F. et al. Increasing the performance of an anion-exchange membrane electrolyzer operating in pure water with a nickel-based microporous layer. *Joule* **5**, 1776–1799 (2021).
17. Lindquist, G. A. et al. Performance and durability of pure-water-fed anion exchange membrane electrolyzers using baseline materials and operation. *ACS Appl. Mater. Interfaces* **13**, 51917–51924 (2021).
18. Krivina, R. A. et al. Anode catalysts in anion-exchange-membrane electrolysis without supporting electrolyte: conductivity, dynamics, and ionomer degradation. *Adv. Mater.* **34**, 2203033 (2022).
19. Tricker, A. W. et al. Design and operating principles for high-performing anion exchange membrane water electrolyzers. *J. Power Sources* **567**, 232967–232976 (2023).
20. Rossi, R., Taylor, R. & Logan, B. E. Increasing the electrolyte salinity to improve the performance of anion exchange membrane water electrolyzers. *ACS Sustain. Chem. Eng.* **11**, 8573–8579 (2023).
21. Zhang, L., Xu, Q., Hu, Y., Chen, L. & Jiang, H. Benchmarking the pH-stability relationship of metal oxide anodes in anion exchange membrane water electrolysis. *ACS Sustain. Chem. Eng.* **11**, 13251–13259 (2023).
22. Osmieri, L. et al. La–Sr–Co oxide catalysts for oxygen evolution reaction in anion exchange membrane water electrolyzer: the role of electrode fabrication on performance and durability. *J. Power Sources* **556**, 232484–232496 (2023).
23. Lee, J. K. et al. Ionomer-free and recyclable porous-transport electrode for high-performing proton-exchange-membrane water electrolysis. *Nat. Commun.* **14**, 4592 (2023).
24. Wang, R. et al. Cathode catalyst layers modified with Brønsted acid oxides to improve proton exchange membrane electrolyzers for impure water splitting. *Nat. Energy* <https://doi.org/10.1038/s41560-41025-01787-41569> (2025).
25. Kong, S. et al. Acid-stable manganese oxides for proton exchange membrane water electrolysis. *Nat. Catal.* **7**, 252–261 (2024).
26. Foglia, F. et al. Disentangling water, ion and polymer dynamics in an anion exchange membrane. *Nat. Mater.* **21**, 555–563 (2022).
27. Li, D. et al. Durability of anion exchange membrane water electrolyzers. *Energy Environ. Sci.* **14**, 3393–3419 (2021).
28. Hu, C. et al. ETFE-grafting ionomers for anion exchange membrane water electrolyzers with a current density of 11.2 A cm⁻². *J. Power Sources* **599**, 234228–234236 (2024).
29. Zheng, Y. et al. Anion exchange ionomers enable sustained pure-water electrolysis using platinum-group-metal-free electrocatalysts. *ACS Energy Lett.* **8**, 5018–5024 (2023).
30. Huang, B. et al. Accelerating gas escape in anion exchange membrane water electrolysis by gas diffusion layers with hierarchical grid gradients. *Angew. Chem. Int. Ed.* **62**, e202304230 (2023).
31. Wu, X., Chen, N., Klok, H. A., Lee, Y. M. & Hu, X. Branched poly(Aryl Piperidinium) membranes for anion-exchange membrane fuel cells. *Angew. Chem. Int. Ed.* **61**, e202114892 (2021).
32. Song, W. et al. Upscaled production of an ultramicroporous anion-exchange membrane enables long-term operation in electrochemical energy devices. *Nat. Commun.* **14**, 2732 (2023).
33. Kraglund, M. R. et al. Ion-solvating membranes as a new approach towards high rate alkaline electrolyzers. *Energy Environ. Sci.* **12**, 3313–3318 (2019).
34. Arunkumar, I. et al. Synthesis of an alkaline-stable in situ cross-linked poly(ether imide)-based anion exchange membrane electrolyte for water electrolyzers and fuel cell applications. *ACS Sustain. Chem. Eng.* **12**, 9361–9375 (2024).
35. Kong, T.-H. et al. In-situ ionomer-free catalyst-coated membranes for anion exchange membrane water electrolyzers. *ACS Energy Lett.* **8**, 4666–4673 (2023).
36. Wang, J. et al. Dynamically adaptive bubbling for upgrading oxygen evolution reaction using lamellar fern-like alloy aerogel self-standing electrodes. *Adv. Mater.* **36**, 2307925 (2023).
37. Zhang, H. et al. Alkaline-stable anion-exchange membranes with barium [2.2.2]cryptate cations: The importance of high binding constants. *Angew. Chem. Int. Ed.* **62**, e202217742 (2023).
38. Chao, T. et al. Reversible hydrogen spillover at the atomic interface for efficient alkaline hydrogen evolution. *Energy Environ. Sci.* **17**, 1397–1406 (2024).
39. Lin, X. et al. Alleviating OH blockage on the catalyst surface by the puncture effect of single-atom sites to boost alkaline water electrolysis. *J. Am. Chem. Soc.* **146**, 4883–4891 (2024).
40. Yao, R. et al. Stable hydrogen evolution reaction at high current densities via designing the Ni single atoms and Ru nanoparticles linked by carbon bridges. *Nat. Commun.* **15**, 2218 (2024).
41. Lu, S.-Y. et al. Synthetic tuning stabilizes a high-valence Ru single site for efficient electrolysis. *Nat. Synth.* **7**, 576–585 (2023).
42. Wan, L. et al. Oriented intergrowth of the catalyst layer in membrane electrode assembly for alkaline water electrolysis. *Nat. Commun.* **13**, 7956 (2022).
43. Yu, P.-C. et al. Nitrogen-mediated promotion of cobalt-based oxygen evolution catalyst for practical anion-exchange membrane electrolysis. *J. Am. Chem. Soc.* **146**, 20379–20390 (2024).
44. Li, Z. et al. Seed-assisted formation of NiFe anode catalysts for anion exchange membrane water electrolysis at industrial-scale current density. *Nat. Catal.* **7**, 944–952 (2024).
45. Klingenhof, M. et al. High-performance anion-exchange membrane water electrolyzers using NiX (X = Fe, Co, Mn) catalyst-coated membranes with redox-active Ni–O ligands. *Nat. Catal.* **7**, 1213–1222 (2024).
46. Lettenmeier, P. et al. Comprehensive investigation of novel pore-graded gas diffusion layers for high-performance and cost-effective proton exchange membrane electrolyzers. *Energy Environ. Sci.* **10**, 2521–2533 (2017).
47. Guo, J. X. et al. Direct seawater electrolysis by adjusting the local reaction environment of a catalyst. *Nat. Energy* **8**, 264–272 (2023).
48. Magaz, G. E., Rodenas, L. G., Morando, P. J. & Blesa, M. A. Electrokinetic behaviour and interaction with oxalic acid of different hydrous chromium(III) oxides. *Croat. Chem. Acta* **71**, 917–927 (1998).
49. Wang, D., Sheng, T., Chen, J., Wang, H.-F. & Hu, P. Identifying the key obstacle in photocatalytic oxygen evolution on rutile TiO₂. *Nat. Catal.* **1**, 291–299 (2018).
50. Li, X. et al. Favoring the originally unfavored oxygen for enhancing nitrogen-to-nitrate electroconversion. *J. Am. Chem. Soc.* **147**, 8587–8596 (2025).
51. Rodríguez, R., Blesa, M. A. & Regazzoni, A. E. Surface complexation at the TiO₂(anatase)/aqueous solution interface: Chemisorption of catechol. *J. Colloid Interface Sci.* **177**, 121–131 (1996).
52. Ze, H. et al. In situ probing the structure change and interaction of interfacial water and hydroxyl intermediates on Ni(OH)₂ surface over water splitting. *J. Am. Chem. Soc.* **146**, 12538–12546 (2024).

53. Qian, Z.-X. et al. Phase engineering facilitates O–O Coupling via lattice oxygen mechanism for enhanced oxygen evolution on nickel-iron phosphide. *J. Am. Chem. Soc.* **147**, 1334–1343 (2024).
54. Zhang, J. et al. Efficient hydrogen production on MoNi₄ electrocatalysts with fast water dissociation kinetics. *Nat. Commun.* **8**, 15437 (2017).
55. Shi, W. et al. Roll-to-roll synthesis of multielement heterostructured catalysts. *Nat. Synth.* <https://doi.org/10.1038/s44160-44025-00758-y> (2025).
56. Liu, J. et al. Elucidating the role of hydroxide electrolyte on anion-exchange-membrane water electrolyzer performance. *J. Electrochem. Soc.* **168**, 054522–054532 (2021).
57. Ng, W., Wong, W., Rosli, N. & Loh, K. Commercial anion exchange membranes (AEMs) for fuel cell and water electrolyzer applications: performance, durability, and materials advancement. *Separations* **10**, 424 (2023).
58. Krivina, R. A. et al. Three-electrode study of electrochemical ionomer degradation relevant to anion-exchange-membrane water electrolyzers. *ACS Appl. Mater. Interfaces* **14**, 18261–18274 (2022).
59. Zhu, Z. et al. A fabrication of iridium oxide film pH micro-sensor on Pt ultramicroelectrode and its application on in-situ pH distribution of 316 L stainless steel corrosion at open circuit potential. *Sens. Actuators B: Chem.* **255**, 1974–1982 (2018).

Acknowledgements

This work was supported by the Natural Science Foundation of China (U25D9010 and U23A2086 to T.L.) and Postdoctoral Science Foundation of China (2025M774230 and GZB20250927 to J.X.G.).

Author contributions

T. Ling conceived the project and designed the experiments. J. X. Guo and R. G. Wang performed the experiments. Y. T. Yang conducted the techno-economic analysis. F. H. Cao and Q. H. Zhang carried out the SECM measurements and fabrication of Pt/IrO₂ UME. J. Zhao performed the Cs-corrected HAADF-STEM. T. Ling, J. X. Guo, and Y. T. Yang wrote the manuscript. C. F. Pan discussed the results and commented on the manuscript.

Competing interests

The authors declare no competing interests.

Additional information

Supplementary information The online version contains supplementary material available at <https://doi.org/10.1038/s41467-026-69053-4>.

Correspondence and requests for materials should be addressed to Yuting Yang, Caofeng Pan or Tao Ling.

Peer review information *Nature Communications* thanks Kenji Miyatake and the other anonymous reviewer(s) for their contribution to the peer review of this work. A peer review file is available.

Reprints and permissions information is available at <http://www.nature.com/reprints>

Publisher's note Springer Nature remains neutral with regard to jurisdictional claims in published maps and institutional affiliations.

Open Access This article is licensed under a Creative Commons Attribution-NonCommercial-NoDerivatives 4.0 International License, which permits any non-commercial use, sharing, distribution and reproduction in any medium or format, as long as you give appropriate credit to the original author(s) and the source, provide a link to the Creative Commons licence, and indicate if you modified the licensed material. You do not have permission under this licence to share adapted material derived from this article or parts of it. The images or other third party material in this article are included in the article's Creative Commons licence, unless indicated otherwise in a credit line to the material. If material is not included in the article's Creative Commons licence and your intended use is not permitted by statutory regulation or exceeds the permitted use, you will need to obtain permission directly from the copyright holder. To view a copy of this licence, visit <http://creativecommons.org/licenses/by-nc-nd/4.0/>.

© The Author(s) 2026